Biomedicine & Pharmacotherapy 173 (2024) 116465

Contents lists available at ScienceDirect

Biomedicine & Pharmacotherapy

journal homepage: www.elsevier.com/locate/biopha

Smart co-delivery of plasmid DNA and doxorubicin using MCM-chitosan-PEG polymerization functionalized with MUC-1 aptamer against breast cancer

Yasaman Esmaeili [a], Arezou Dabiri [b], Fariba Mashayekhi [c], Ilnaz Rahimmanesh [b], Elham Bidram [a,c], Saeed Karbasi [c], Mohammad Rafienia [a], Shaghayegh Haghjooy Javanmard [b], Yavuz Nuri Ertas [d,e,f], Ali Zarrabi [g], Laleh Shariati [b,c,*]

[a] Biosensor Research Center (BRC), Isfahan University of Medical Sciences, Isfahan, Iran
[b] Applied Physiology Research Center, Cardiovascular Research Institute, Isfahan University of Medical Sciences, Hezarjerib Ave, Isfahan 8174673461, Iran
[c] Department of Biomaterials, Nanotechnology and Tissue Engineering, School of Advanced Technologies in Medicine, Isfahan University of Medical Sciences, Iran
[d] Department of Biomedical Engineering, Erciyes University, Kayseri 38039, Turkiye
[e] ERNAM—Nanotechnology Research and Application Center, Erciyes University, Kayseri 38039, Turkiye
[f] UNAM–National Nanotechnology Research Center, Bilkent University, Ankara 06800, Turkiye
[g] Department of Biomedical Engineering, Faculty of Engineering and Natural Sciences, Istinye University, Sariyer, Istanbul 34396, Turkey

ARTICLE INFO

Keywords:
Gene delivery
Drug delivery
Breast Cancer
Smart Co-delivery
Targeted therapy

ABSTRACT

This study introduces an innovative co-delivery approach using the MCM-co-polymerized nanosystem, integrating chitosan and polyethylene glycol, and targeted by the MUC-1 aptamer (MCM@CS@PEG-APT). This system enables simultaneous delivery of the GFP plasmid and doxorubicin (DOX). The synthesis of the nanosystem was thoroughly characterized at each step, including FTIR, XRD, BET, DLS, FE-SEM, and HRTEM analyses. The impact of individual polymers (chitosan and PEG) on payload retardation was compared to the co-polymerized MCM@CS@PEG conjugation. Furthermore, the DOX release mechanism was investigated using various kinetic models. The nanosystem's potential for delivering GFP plasmid and DOX separately and simultaneously was assessed through fluorescence microscopy and flow cytometry. The co-polymerized nanosystem exhibited superior payload entrapment (1:100 ratio of Plasmid:NPs) compared to separately polymer-coated counterparts (1:640 ratio of Plasmid:NPs). Besides, the presence of pH-sensitive chitosan creates a smart nanosystem for efficient DOX and GFP plasmid delivery into tumor cells, along with a Higuchi model pattern for drug release. Toxicity assessments against breast tumor cells also indicated reduced off-target effects compared to pure DOX, introducing it as a promising candidate for targeted cancer therapy. Cellular uptake findings demonstrated the nanosystem's ability to deliver GFP plasmid and DOX separately into MCF-7 cells, with rates of 32% and 98%, respectively. Flow cytometry results confirmed efficient co-delivery, with 42.7% of cells showing the presence of both GFP-plasmid and DOX, while 52.2% exclusively contained DOX. Overall, our study explores the co-delivery potential of the MCM@CS@PEG-APT nanosystem in breast cancer therapy. This system's ability to co-deliver multiple agents preciselyopens new avenues for targeted therapeutic strategies.

1. Introduction

Cancer, especially breast cancer, poses a significant challenge to modern medicine due to its complexity and varied nature. To address this, researchers have turned to innovative treatments, such as co-delivery systems [1,2]. These systems are designed to carry and release multiple therapeutic agents—like genes and drugs—directly to cancer cells, aiming to improve treatment outcomes while minimizing side effects [3].

Gene therapy is a critical component of these strategies. It targets cancer at a genetic level, offering the potential for highly precise treatments [4]. However, delivering therapeutic genes accurately to cancer

* Corresponding author at: Applied Physiology Research Center, Cardiovascular Research Institute, Isfahan University of Medical Sciences, Hezarjerib Ave, Isfahan 8174673461, Iran.
E-mail address: shariati_l59@yahoo.com (L. Shariati).

https://doi.org/10.1016/j.biopha.2024.116465
Received 24 December 2023; Received in revised form 11 March 2024; Accepted 15 March 2024

cells without affecting healthy ones is a major hurdle [5,6]. This has led to the development of advanced delivery mechanisms, such as smart delivery systems that can intelligently release their therapeutic payload at the right place and time [7,8]. Chitosan, a naturally occurring biopolymer, stands out in this context for its ability to change behavior in different environments, making it particularly useful for targeting the acidic surroundings of tumor cells [9].

In a research study, nanoparticles made of poly-(lactic-co-glycolic acid) were coated with chitosan using its pristine structure [10]. Fluorescein isothiocyanate-labeled CRISPR/Cas9 complex was delivered via this method, and subsequent cellular uptake investigations suggested that the complex was inside the nucleus of cells. Furthermore, using the CRISPR/Cas9 plasmid delivery system to treat the human embryonic kidney cell line caused the expression of green fluorescence protein to be 80% suppressed [10].

On the other hand, mesoporous silica nanoparticles, specifically MCM-41, have recently established as a promising platform for gene and drug delivery. MCM-41 possesses unique physicochemical attributes, high biocompatibility, and tunable pore sizes. These characteristics have made it a subject of increasing interest in both gene and drug delivery for its ability to protection nucleic acids and drug molecules [11,12]. In our more recent study, we developed a drug delivery system based on mesoporous silica@chitosan@gold nanosystem to enhance delivery of curcumin into breast and colon tumor cells. In this research, it was shown that the pores on the surface of MCM-41 enhance drug loading onto the nanosystem, and the presence of pH-sensitive chitosan nanoparticles creates a smart nanosystem, eventually leading to the delivery of more curcumin into the desired cells [13].

Aptamers have also emerged as a promising targeted class of molecular recognition agents for cancer cell targeting that can be used to selectively target cancer cells or tumor-associated biomarkers [14–16]. Mucin 1 (MUC-1) targeting aptamers can selectively bind to the MUC-1 protein found on the surface of many cancer cells. By specifically targeting cancer cells, MUC-1 aptamers can be used as a powerful tool for cancer diagnosis and treatment while avoiding non-cancerous cells, reducing side effects and increasing the efficacy of treatment [17,18]. It is noteworthy to mention that in our recent studies we used molecular dynamics simulations to evaluate the interaction of payloads with the MUC-1 aptamer. It was indicated that when the aptamer specifically binds to the MUC-1 receptor, its double strands separate under the low pH condition, leading to the drug release [13,19,20]. Overall, the use of MUC-1 aptamers in cancer cell targeting holds great promise for improving cancer diagnostics and therapeutics.

In the current project, we explore the potential of a co-delivery nanosystem based on MCM-41. We modified this system with a copolymer of chitosan-poly ethylene glycol (PEG) and then functionalized it with MUC-1 aptamer-targeting molecules, enhancing its specificity. Incorporating doxorubicin (DOX), a potent chemotherapy drug, into the proposed co-delivery system further boosts its therapeutic potential. The addition of DOX to our co-delivery nanosystem not only enhances gene therapy but also takes advantage of the drug's proven success in treating breast cancer.

Overall, this study aims to evaluate the effectiveness of this smart co-delivery nanosystem in the context of breast cancer therapy. By using the advantages of smart delivery systems, harnessing the potential of gene therapy, exploiting on DOX's efficacy, and integrating chitosan-PEG copolymerization, holds promise for the future of next-generation pharmaceutics in breast cancer.

2. Materials and methods

2.1. Materials

Cetrimonium bromide (CTAB), tetraethyl orthosilicate (TEOS), Polyethylene glycol- maleimide (PEG-Mal), and chitosan of low molecular weight were procured from Sigma in the United States. 1,4-Dithiothreitol (DTT) and Doxorubicin were obtained from Merck in Germany. The AddBio AddPrep Genomic DNA extraction kit was acquired from Sinaclon in Iran. Dulbecco's modified Eagle medium (DMEM), penicillin/streptomycin (pen/strep), and trypsin-EDTA enzyme were supplied by Gibco in the USA. Additionally, 3-(4, 5-Dimethylthiazol-2-yl)-2, 5-diphenyltetrazolium bromide (MTT) and fetal bovine serum (FBS) were procured from Sigma, USA. The aptamer used (sequence: 5′-GCCCGCCGTGGCTGGGTCTTCCTTGGTCGGTCTACAAAAAAAAAA-SH-3′) was obtained from SBS Genetech Co. Ltd. The MCF-7 breast cancer cell line was acquired from the Pasteur Institute of Iran

2.2. Characterization study

The physicochemical attributes of the nanoconjugate produced at each stage were evaluated through several analytical techniques. Fourier-transform infrared spectroscopy (FTIR) was employed for spectral analysis, using a JASCO 6300 instrument from Japan. X-ray diffraction (XRD) patterns were acquired using an Asenware AW-DX300 instrument from Germany to probe the crystalline structure. Surface morphology and structure were visualized using scanning electron microscopy (SEM) performed on a TESCAN MIR3 instrument from the Czech Republic, as well as high-resolution transmission electron microscopy (HRTEM) conducted with a JEOL JEM-ARM200CFEG UHR-TEM instrument from Japan. Furthermore, the Brunauer–Emmett–Teller (BET) analysis was utilized to study the specific surface area. The particle size distribution and surface charge of the nanosystem were determined using a Zeta sizer (HORIBA, scientific SZ100) from Japan.

2.3. Preparation of MCM@CS@PEG-APT nanosystem

The MCM-41 nanoparticles were synthesized through sol-gel method in alkaline medium as previously reported in our study [13]. In the subsequent step, a chitosan and PEG polymer solution was meticulously prepared with a weight ratio of 1:1 (w/w). This prepared solution was then added drop by drop to the MCM-41 solution at a ratio of 1:2 (MCM: Co-polymer, w/w). Suspended MCM-41 was then exposed under sonication and stirrer for 12 h. The product, MCM@CS@PEG, was obtained by purifying the crude product using dialysis (MW cut off = 12,000 Da). To synthesize the final MCM@CS@PEG-APT nanoconjugate, Mucin-1 (MUC-1) aptamer was added according to our previous study [19], in which the aptamer thiol (–SH) tail was first activated with DTT, while the activated aptamer was mixed with MCM@CS@PEG solution and linked to the maleimide groups on the PEG via covalent bond. Finally, the MCM@CS@PEG-APT was washed with buffer and was stored at 4 °C for future use.

2.4. Loading Doxorubicin into the nanoconjugate

Doxorubicin (DOX) was solubilized in a phosphate buffer solution with a pH of 7.4 and subsequently combined with the aqueous dispersion of MCM@CS@PEG-APT at weight ratios of 1:1, 1:2, and 2:1 (nanosystem to DOX). This mixture was vigorously agitated for a period of 24 hours. The concentration of pure DOX was determined by generating a standard curve, which involved measuring the UV absorbance at 488 nm for a series of DOX solutions with known concentrations in a phosphate buffer. The DOX-loading capacity and entrapment efficiency were then calculated using the following equations:

$$\%\text{Loading capacity (LC)} = \frac{\text{Total DOX added (wt)} - \text{DOX unentrapped (Wt)}}{\text{Total nanocarrier (wt)}} x100 \quad (1)$$

$$\%\text{Entrapment efficiency(EE)} = \frac{\text{Total DOX added(wt)} - \text{DOX unentrapped(Wt)}}{\text{Total DOX added(wt)}} x100 \quad (2)$$

2.5. Loading GFP plasmid into the nanoconjugate

In order to conduct an investigation of the GFP (green fluorescent protein) plasmid binding affinity, 2 μg of plasmid was combined with varying concentrations of the nanoconjugates MCM@CS, MCM@PEG, and MCM@CS@PEG in deionized (DI) water at various weight/weight (w/w) ratios of plasmid DNA to NPs (1:10–1:640). The complexes were examined by electrophoretic mobility in 1% agarose gel at a voltage of 110 V for 30 min after 30 min of incubation. A UV transilluminator was used to capture the images.

2.6. Stability assay of the nanoconjugate

The DNase I assay was employed as a model to assess the protective capabilities of MCM@CS@PEG (GFP) polyplexes against *in vivo* nucleases. Polyplexes, prepared with a Plasmid: NPs ratio of 100, along with a naked GFP plasmid solution were subjected to a series of treatments. Each sample was combined with 0.45 μl of DNase I and 1 μl of a 10X reaction buffer containing $MgCl_2$. The resulting mixtures were then incubated for durations of 10, 30, and 60 minutes at 37°C. After each respective incubation period, samples were incubated to 75°C for an additional 10 minutes for inactivating DNase. Subsequently, agarose gel electrophoresis (1%) was conducted following standard procedures. The gel results obtained from the DNase I assay were analyzed using the UV transilluminator (National Institute of Health, Bethesda, Maryland, USA). This experimental setup allowed for the evaluation of the protective effect of MCM@CS@PEG polyplexes against nucleases in a controlled environment.

Furthermore, the integrity of the polyplexes was assessed in the presence of a competing polyanion, specifically heparin. To conduct this evaluation, MCM@CS@PEG (GFP) polyplexes containing 2 μg of GFP plasmid at a Plasmid: NPs ratio of 1:100 were subjected to incubation with heparin solutions of varying concentrations, ranging from 50 to 5000 heparin IU/ml. This incubation process occurred at 37°C for a duration of 30 minutes. Following incubation, the samples were analyzed using agarose gel electrophoresis, which was carried out at 100 V for 35 minutes. The outcomes of the heparin competition assay were subsequently analyzed using a UV transilluminator. This assay allowed for the examination of polyplex stability under conditions of competition with heparin, providing insights into their behavior in the presence of polyanions.

2.7. Cell compatibility assay

Cell viability was assessed using the MTT colorimetric assay. In this study, MCF-7 cells, which overexpressd the MUC-1 receptor, were used as the positive control. Different plasmid-to-nanoparticle (NPs) ratios (1:25, 1:50, 1:100, 1:150, 1:200, 1:250, 1:300) were applied to treat the cell lines with MCM@CS@PEG-APT and MCM@CS@PEG-APT (DOX-GFP) for durations of 24 and 48 hours. As a reference, pure Doxorubicin (50 μg/ml) and untreated cells were used as the positive and negative controls, respectively. The absorbance was measured at 490 nm using an ELISA reader from Biorad, USA.

2.8. Drug release and kinetic assay

To assess the *in vitro* drug release profile, MCM@CS@PEG-Apt (DOX) nanoparticles (1% wt.) were dispersed in phosphate-buffered saline (PBS) at two different pH values, 5.5 and 7.4, and agitated at 37°C. At predetermined intervals, the buffer solution in the vials was collected for UV-Vis analysis at 488 nm, and fresh buffer solution was added in place of the collected sample. The drug release percentage was calculated using the following formula:

$$\%\textbf{Drug release} = \frac{\text{The amount of drug release(wt)}}{\text{Total amont of curcumin in the nanoconjugate(wt)}} \times 100 \quad (3)$$

Next, we systematically investigated the kinetics of DOX release using various models, including Zero-order, First-order, Korsmeyer-Peppas, and Higuchi models. To identify the most appropriate kinetic model for DOX release, data fitting was performed using Grafpad Prism software. Subsequently, the regression coefficient (R2) was utilized to determine the model that best describes the release of DOX over time. In all the equations that follow, "Mt" represents the quantity of DOX released at a specific time point:

$$\textbf{\textit{Zero order model}}: M_t = \mathrm{Kt} \quad (4)$$

Where *K* is the zero-order kinetic constant.

$$\text{First } \textbf{\textit{order model}}: M_t = -\mathrm{Kt} \quad (5)$$

Where *K* is the first order kinetic constant.

$$\textbf{\textit{Korsmeyer}} - \textbf{\textit{Peppas}}: M_t = \mathrm{Kt}^n \quad (6)$$

Where *K* is the Korsmeyer-Peppas constant, and n is the release exponent that shows the drug release mechanism.

$$\textbf{\textit{Higuchi}}: M_t = \mathrm{Kt}^{0/5} \quad (7)$$

Where *K* is the Higuchi constant.

2.9. Cellular uptake assay

MCF-7 cells were seeded in 6-well plates at a density of 4×10^5 cells per well. After 24 hours, the cells were transfected with various conjugates, including MCM@CS@PEG-APT, MCM@CS@PEG-APT (GFP), MCM@CS@PEG-APT (DOX), and MCM@CS@PEG-APT (GFP-DOX), using a plasmid-to-NPs ratio of 100. To enhance transfection efficiency, the culture medium was replaced with 250 μl of serum-free RPMI 1640. Subsequently, polyplexes were added to the wells and incubated for 5 hours. Finally, the cell culture medium was replaced with fresh complete medium. Additionally, the transfection efficiency of lipofectamine 3000 combined with GFP plasmid and pure DOX was evaluated as positive controls following the manufacturer's instructions. After 24 hours, the transfected cells were observed using fluorescence microscopy (Nikon-TE2000-U, Japan). And, for flow cytometry analysis, cells were washed with PBS and detached using trypsin-EDTA for 5 minutes in an incubator. Once trypsin-EDTA action was neutralized, cells were centrifuged at 1500 rpm for 5 minutes and resuspended in PBS (pH 7.4). Flow cytometry analysis (Calibur, BD, USA) was employed to assess transfection results, utilizing fluorescence channel 1 (FL-1) to detect GFP plasmid and fluorescence channel 2 (FL-2) to detect DOX.

2.10. Statistical study

GraphPad Prism software version 9 and SPSS software (version 21) were employed for quantitative data analysis. Non Parametric analysis

of variance (Mann–Whitney U test) was performed for statistical comparisons. The results are presented as mean values with accompanying standard deviations (SD), and statistical significance was determined at a threshold of $P_{value} \leq 0.05$

3. Results and discussion

In this investigation, an innovative codelivery nanosystem was designed and fabricated that demonstrates the ability to efficiently transport two distinct therapeutic payloads: a plasmid containing the GFP gene and the potent anticancer agent Doxorubicin. The main foundation of this nanosystem is composed of MCM-41 that have been coated with a co-polymer including chitosan and polyethylene glycol (PEG). This precise material integration offers a multifaceted platform that could improve the delivery of targeted genes and drugs for the treatment of cancer.

Mesoporous silica nanoparticles (MCM-41) were chosen as the primary component of this nanosystem due to a number of benefits they provide. Their inherent high drug loading capacity allows the efficient encapsulation of both the GFP gene plasmid and Doxorubicin, enabling a multifaceted therapeutic approach [21]. Additionally, MCM-41's high surface area provides sufficient surface for loading substantial drug payloads, while the customizable pore size offers control over drug release kinetics, a crucial factor in optimal therapeutic effects. However, the interaction between MCM-41's silanol groups (Si-OH) and cellular membranes poses potential toxicity concerns, demanding the necessity for modifications to enhance biocompatibility within biological systems [22]. This challenge is addressed, in this project, through the incorporation of a chitosan-PEG coating. This combination not only reduces potential systemic toxicity associated with MCM-41 but also causes controlled and sustained release of drug molecules, thereby enhancing treatment efficacy. Furthermore, the chitosan-PEG coating facilitates precise targeting by minimizing steric hindrance between targeting ligands and biomarkers, thus enhancing the accuracy of therapeutic delivery [23].

The integration of targeted MUC-1 aptamers into the nanosystem could specifically recognise and bind to the MUC-1 antigen, which is overexpressed on breast tumor cells. This targeted approach enables not only high specificity in detecting cancer biomarkers but also ensures the precise delivery of therapeutic agents to the tumor site [24,25]. The synergistic integration of the designed nanosystem's components, including MCM-41's capabilities, chitosan-PEG's biocompatibility enhancement, and the precise targeting potential of the MUC-1 aptamer, yields a multifunctional platform with notable benefits. Scheme 1 illustrates the step-by-step fabrication of the nanosystem.

3.1. Characterization study

The comprehensive analysis of chemical composition and interfacial interactions throughout each stage of nanosystem synthesis was conducted via FTIR spectroscopy. In Fig. 1**A**, the FTIR spectra of four pivotal phases in the nanosystem's progression are presented: MCM-41, MCM@CS, MCM@CS@PEG, and MCM@CS@PEG-APT (DOX). The FTIR spectrum of MCM-41 reveals distinct characteristics, including a broad band at 3440 cm^{-1} corresponds to O–H group stretching vibrations. Additionally, peaks at 1090 cm^{-1}, 972 cm^{-1}, and 468 cm^{-1} align with Si-O-Si, Si-OH, and Si-O groups respectively, revealing the MCM-41's silica framework and surface functionality [26]. The FTIR spectrum of MCM@CS demonstrates new bands at around ~3620 cm^{-1} and ~3200 cm^{-1}, attributed to –OH and –NH stretching vibrations [27]. Further, the peak at 1648 cm^{-1} can be attributed to $–CH_2$ deformation vibrations of the quaternary ammonium group. These shifts validate the

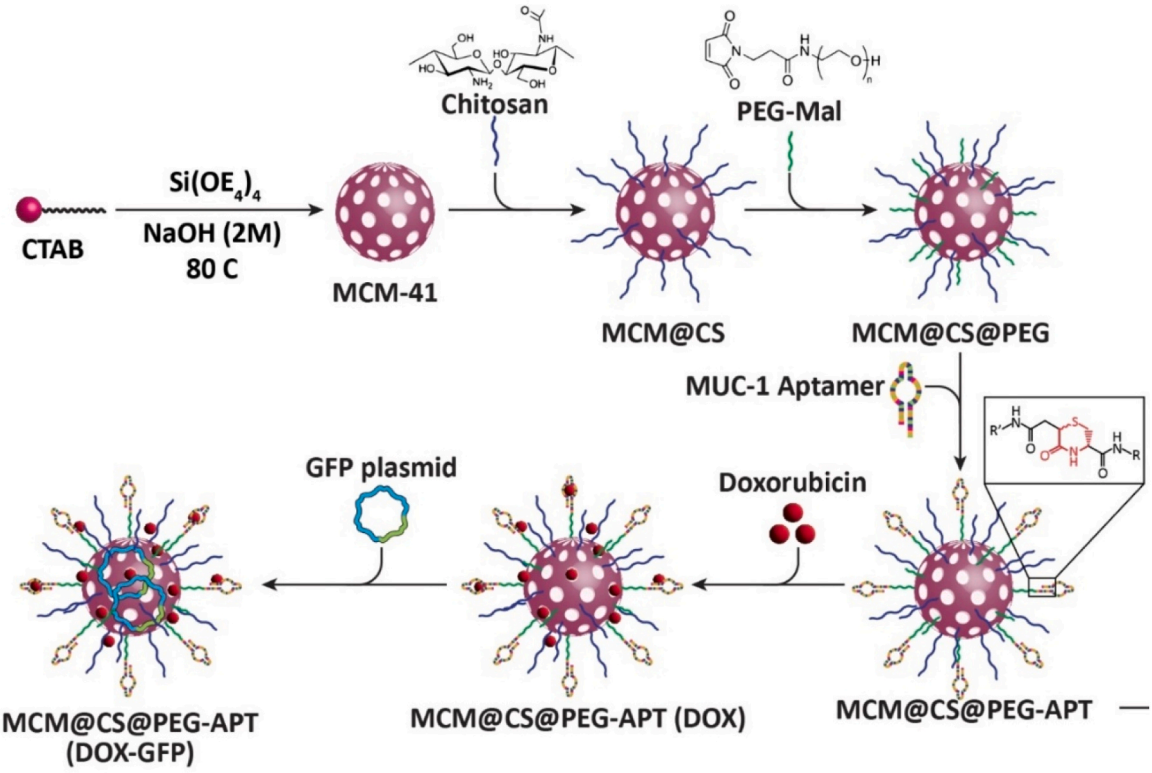

Scheme 1. Stepwise schematic of the nanosystem synthesis: First, MCM-41 was synthesized using a surfactant-assisted sol-gel method. Subsequently, the surface of MCM-41 was modified with a copolymer of chitosan and polyethylene glycol-maleimide (PEG-Mal). In the next stage, the MUC-1 aptamer, serving as a targeted agent, was attached to PEG-Mal through ester bonds, resulting in the formation of MCM@CS@PEG-APT. Following aptamer attachment, the anticancer drug DOX was loaded into the nanosystem, yielding the final nanosystem denoted as MCM@CS@PEG-APT (DOX). Finally, the GFP plasmid was introduced into the nanoconjugate, creating a co-delivery platform termed MCM@CS@PEG-APT (DOX-GFP) for combined therapeutic and genetic payload delivery.

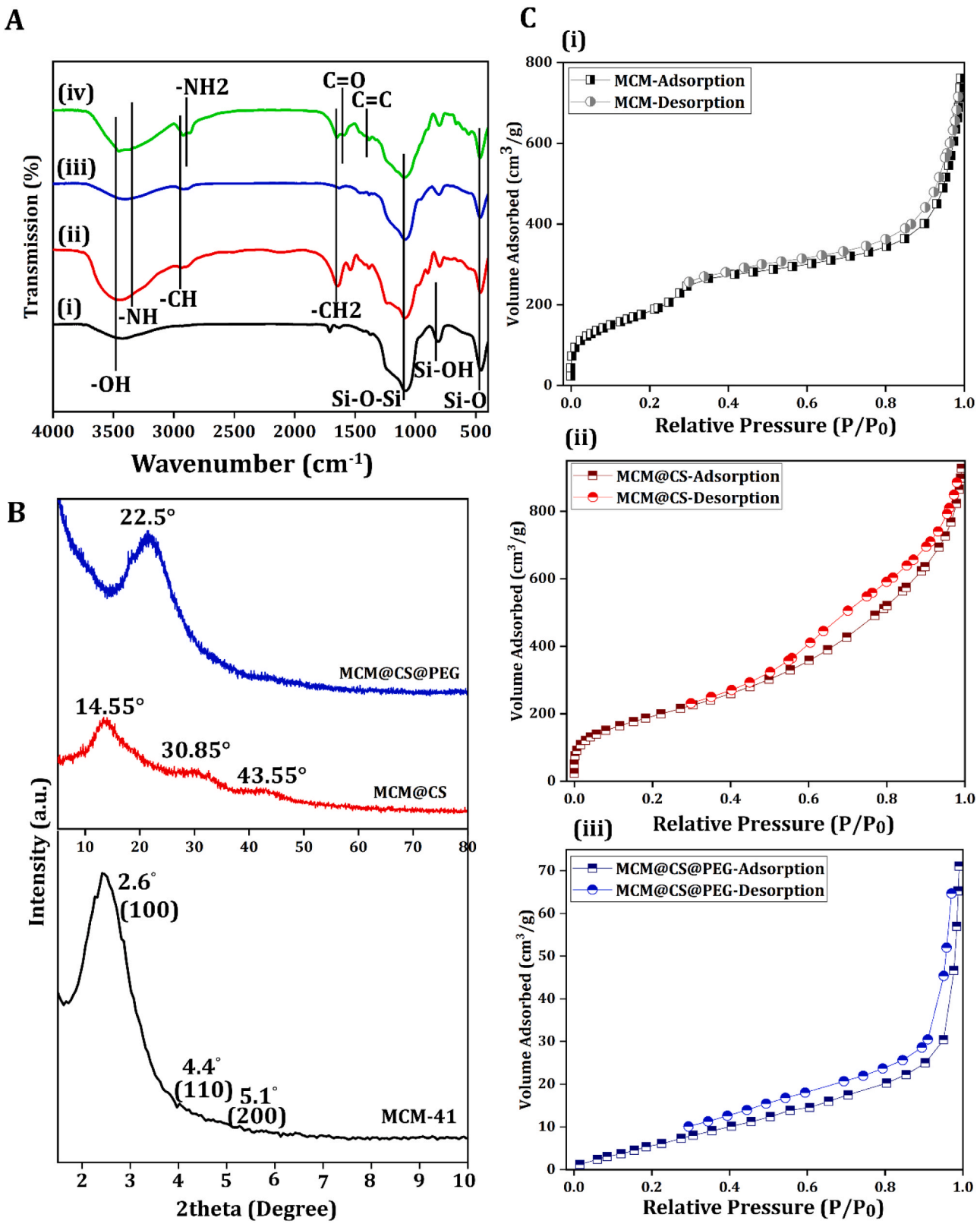

Fig. 1. **(A)** The FTIR spectra of nanoconjugates: (i) MCM-41, MCM@CS, MCM@CS@PEG, MCM@CS@PEG-APT(DOX), **(B)** The XRD patterns of MCM-41, MCM@CS, MCM@CS@PEG, **(C)** the N_2 adsorption/desorption isotherms and the pore size distributions of MCM-41 and MCM@CS, and MCM@CS@PEG conjugates.

successful chitosan modification of MCM-41 and the presence of corresponding functional groups. The FTIR analysis confirmed the physical interactions between MCM and PEG, particularly through the identification of a distinct absorption band for PEG's aliphatic CH groups within the 2800–3000 cm^{-1} range [28]. This band indicates the presence of methylene (CH_2) groups in the PEG chain and suggests that the MCM-41's major pore structure is maintained in the MCM@CS@PEG formulation [29]. Regarding the presence of DOX into the nanosystem,

the FTIR spectrum of MCM@CS@PEG-Apt (DOX) confirms DOX presence through distinct absorption bands at around 1650 cm^{-1}, indicative of significant C═O stretching vibrations inherent to amide groups [30]. Characteristic absorption bands within the 1500–1600 cm^{-1} range correspond to C═C stretching vibrations, obviously confirming the presence of the aromatic ring structure. Detection of these absorption bands in the FTIR spectrum of the loaded nanosystem firmly affirms the successful encapsulation of DOX within the nanosystem.

The crystal structures of MCM-41, MCM@CS, and MCM@CS@PEG were precisely examined using X-ray diffraction (XRD), and the results are depicted in Fig. 1B. In the low-angle XRD pattern of MCM-41, distinct peaks were observed, including a prominent reflection peak at $2\theta = 2.6°$, associated with the (100) plane, along with two relatively weaker reflection peaks at $2\theta = 4.4°$ and 5.1°, corresponding to the (110) and (200) planes, respectively. These peaks serve as characteristic indicators of the 2D mesoporous silica structure [31]. The interaction of chitosan with MCM-41 (MCM-41@CS) led to emerge new peaks at $2\theta =$ 14.55°, 30.85°, and 43.55°, confirming the presence of chitosan in the nanostructure [32]. On the other hand, the XRD pattern of MCM@CS@PEG demonstrated broader diffraction bands at $2\theta = 22.5°$, indicating an increased level of amorphous character [33]. Remarkably, the influence of MCM-41 on the arrangement of the PEG molecular chain within the polymer's crystal lattice was evident. This effect disrupted the crystalline order of PEG, thereby validating the effective conjugation of PEG to MCM-41 through physical interactions.

Fig. 1C illustrates the N_2 adsorption/desorption isotherms for MCM-41, MCM-41 functionalized with chitosan (MCM@CS), and MCM@CS functionalized with PEG (MCM@CS@PEG). The isotherms exhibited a type-IV pattern based on the IUPAC classification, confirming the presence of a characteristic mesoporous structure in the synthesized materials [34]. Additionally, the Barrett-Joyner-Halenda model (BJH) analysis revealed a narrow pore size distribution, as depicted in Fig. 1C. The pore diameters (DBJH), BET surface area (BET), and total pore volumes (V_{total}) properties of MCM-41, MCM@CS, and MCM@CS@PEG conjugates are summarized in Table 1. Notably, the functionalization of the MCM-41 surface with chitosan and PEG resulted in reduced pore volume, surface area, and pore size values, suggesting that these polymers modified the surface characteristics of MCM-41

The loading of doxorubicin into the nanosystem followed incorporated into the final nanoconjugate known as MCM@CS@PEG-APT. Computational modeling in our previous work study demonstrated that DOX intercalates into the double-stranded regions of the aptamers through non-covalent interactions, in addition to being adsorbed into the mesoporous pores of the nanosystem [19]. The loading capacity of DOX and its entrapment efficiency were determined by quantifying the adsorbed pure DOX post-loading, with measurements carried out using a standard curve relationship with DOX in PBS [19]. Consequently, a 1:1 ratio between the nanosystem and DOX with 99.42% loading capacity and entrapment efficiency was selected as the optimal ratio for further investigations (Table 2).

Table 3 presents the surface charge and the average hydrodynamic radius of the nanosystem at different stages of synthesis. Initially, MCM-41 exhibited a negative charge of approximately −60 mV, owing to the presence of sulfide groups on its surface. Following the surface modification with chitosan, the negative charge was reduced to around −12 mV. The introduction of PEG in the synthesis of MCM@CS@PEG further shifted the ζ-potential to approximately −1.5 mV due to the NH groups of the maleimide in the end of PEG. Subsequently, the attachment of aptamers to the nanoconjugate increased the ζ-potential to −12.3 mV, primarily due to the negative charge of DNA. However, the loading of DOX into the final nanoconjugate altered the ζ-potential to −4.1 mV (with a PDI of 0.25), primarily due to its positive charge. In summary, these results indicate the formation of a moderately stable final suspension, characterized by proper dispersibility. This is advantageous for stability, as uniform particle sizes tend to exhibit more predictable interactions and have a reduced tendency to aggregate or settle. The hydrodynamic size of MCM-41 and MCM@CS falls within the range of 200–300 nm. In contrast, the average hydrodynamic size of MCM@CS@PEG, MCM@CS@PEG-APT, and MCM@CS@PEG-APT (DOX) is less than 1 μm.

Further analysis encompassed the utilization of HRTEM and FE-SEM techniques to demonstrate the morphology, textural attributes, and distribution of elements within the nanoconjugates. HRTEM images of MCM-41 indicated homogenous nanospheres arranged in a hexagonal pattern, complete with channel structures (Fig. 2**A**). The MCM@CS@PEG nanoconjugate similarly presented spherical nanoparticles of distinct form, highlighting the successful grafting of CS@PEG onto the MCM-41 framework, thereby preserving its internal porous configuration (Fig. 2**B**).

Furthermore, examination of the final nanoconjugates through FE-SEM, as presented in Fig. 3**A**, revealed consistently dispersed and uniform nanospheres, with an average diameter ranging from 10 to 13 nm. The conclusive chemical composition analysis of the ultimate nanosystem (MCM@CS@PEG-APT (DOX)) was accomplished through EDAX point analysis. This study provided a comprehensive conception of the element distribution on the surface, confirming the presence of carbon (C), oxygen (O), nitrogen (N), and sulfur (S) (Fig. 3**B**). Accordingly, C and O were in accord with the MCM-41 matrix; N was attributed to the chitosan, PEG, and DOX; and the presence of S aligned with the aptamer-confirming the forming a linkage at the aptamer terminus (Fig. 3**C**).

Table 1
Total pore volumes (V_{total}), BET surface area (SBET), and Pore diameters (DBJH) from N2 adsorption–desorption isotherms for MCM-41, and MCM@CS, and MCM@CS@PEG.

Nano-conjugate	BET pore volume (cm^3/g)	BET surface area (m^2/g)	BJH pore diameter (nm)
MCM-41	1.1571	705	1.9
MCM@CS	1.04	678	1.64
MCM@CS@PEG	0.1088	32.86	1.2

Table 2
Comparison of the loading capacity and the entrapment efficiency of different ratio of nanosystem and drug.

Nanoconjugate	Ratio (Nanosystem: Drug)	Loading capacity (%)	Entrapment efficiency (%)
MCM@CS@PEG-APT(DOX)	1:1	99.42	99.42
	1:2	48.7	97
	2:1	190	99.3

Table 3
The zeta potential and the hydrodynamic radius size of nanoconjugates.

Nanoconjugate	Zeta (ζ) potential (mV)	Hydrodynamic radius size (nm)
MCM-41	-60	345
MCM@CS	-12	360
MCM@CS@PEG	-1.5	<1 μm
MCM@CS@PEG-APT	-12.3	<1 μm
MCM@CS@PEG-APT (DOX)	-4.1	<1 μm

3.2. Retardation and Stability Study

The nanoconjugate was used as a carrier to adsorb plasmid via electrostatic adsorption to perform plasmid delivery. The interactions between the nanoconjugate and GFP-plasmid were analyzed by electrophoretic mobility in 1% agarose gel with various weight/weight (w/w) ratios of GFP-plasmid DNA to NPs (Fig. 4**A**). Here, the comparative analysis of MCM-41 functionalized with individual polymers—chitosan

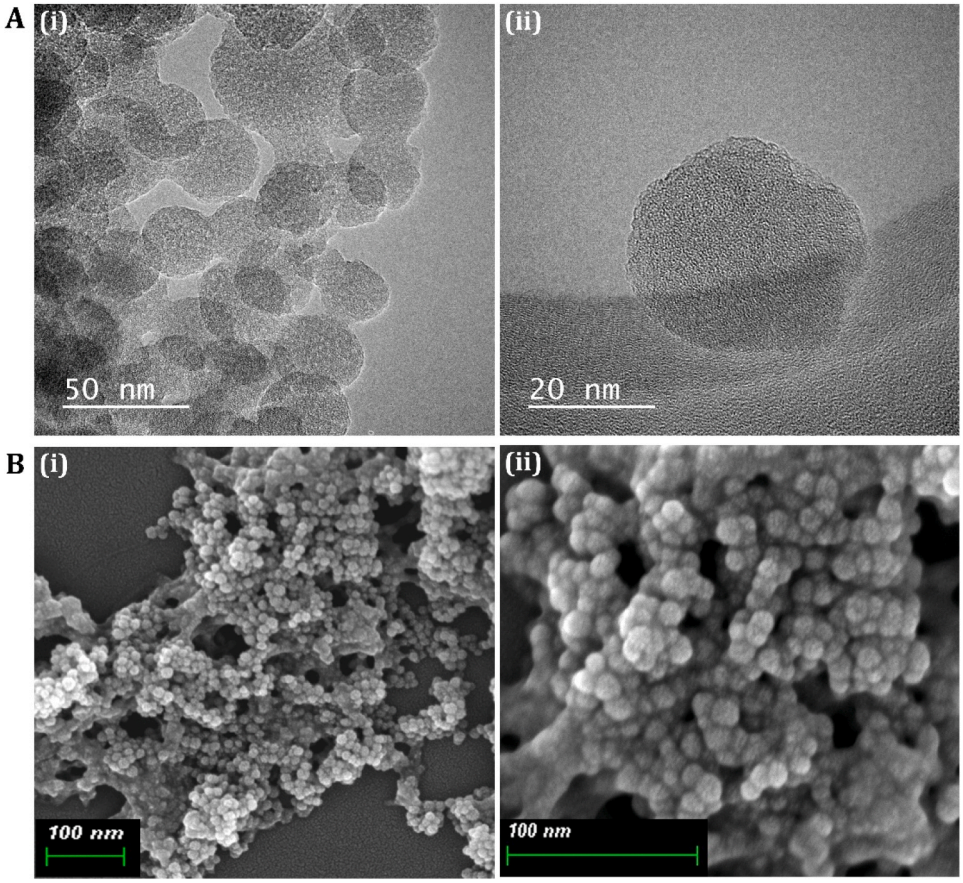

Fig. 2. (A) HRTEM images of MCM-41 with (i) 50 nm and (ii) 20 nm magnification, **(B)** The FE-SEM micrographs of MCM@CS@PEG nanoconjugates with two different magnifications. Scale bar, 100 μm.

and PEG—versus the co-polymerized MCM@CS@PEG was evaluated. The results of investigation revealed that both chitosan-functionalized MCM-41 and PEG-functionalized MCM-41 significantly enhanced payload retention compared to bare MCM-41. As demonstrated in Fig. 4**A**, naked plasmid as a negative control showed a sharp band compared to the other bands that their intensity was reduced with increasing weight ratios (GFP-plasmid/NPs). Besides, it was revealed that plasmid could bind with MCM@CS and MCM@PEG to form stable DNA-nanoconjugate complexes (polyplexes) at weight ratios larger than 1:640 because no free plasmid was detected. However, the co-polymerized MCM-41, MCM@CS@PEG, absorb plasmid at the ratio (1:100), confirming that the plasmid was entrapped in the well containing MCM@CS@PEG and completely disappeared in the supernatant. Hence, the MCM@CS@PEG configuration exhibited a remarkable reduction in payload retardation compared to the individual polymer-coated complements. This was attributed to the balanced interplay between chitosan and PEG, which collectively optimized the release kinetics of the payloads [35]. Notably, the retarded movement of plasmid entrapped in the nanoconjugate on agarose gel showed that MCM@CS@PEG, as delivery carrier, can condense plasmid efficiently.

Gene delivery carriers play a pivotal role in protecting DNA payloads against degradation, a fundamental factor for their efficacy in therapeutic applications. In this study, the ability of the designed nanocarrier, MCM@CS@PEG polyplexes, to shield GFP-plasmid DNA from degradation by employing DNase I as a model enzyme was assessed. In Fig. 4**B**, Lane 1 serves as a DNA marker, offering a reference point for the molecular weight of the GFP-plasmid, and lane 2 is the naked GFP-plasmid. Lanes 3, 4, and 5 show the naked GFP-plasmid exposed to DNase I for 10, 30, and 60 minutes, respectively. Conversely, lanes 7, 8, and 9 display the MCM@CS@PEG polyplexes loaded with GFP-plasmid (GFP-plasmid/NP ratio: 100) subjected to the same DNase I treatment over the same time intervals.

The bands corresponding to the naked GFP-plasmid, seen in lanes 3, 4, and 5, are progressively demolished with increasing exposure time to DNase I. In contrast, the bands representing the MCM@CS@PEG polyplexes in lanes 7, 8, and 9 exhibit not reduction in intensity. This stark contrast in the susceptibility to DNase I degradation between naked GFP-plasmid and the polyplex-encapsulated GFP-plasmid highlights the effectiveness of the designed nanocarrier system. Notably, the MCM@CS@PEG polyplexes successfully preserved the integrity of the GFP-plasmid for a duration of up to 60 minutes. The remarkable stability observed in the polyplex-encapsulated GFP-plasmid can be attributed to the robust ionic bonding interactions that occur within the nanocarrier system [36]. Specifically, the amino groups present in chitosan PEG interact strongly with the phosphate groups of the DNA plasmid. This interaction forms a protective shield around the genetic material, preventing its degradation by nucleases [37].

In another crucial stability assessment, MCM@CS@PEG polyplexes were created at a plasmid/NPs ratio of 100 and exposed to varying concentrations (5–5000 IU/ml) of heparin, a highly charged polyanion known for its interaction with nucleic acids and various nanoparticles. In the gel electrophoresis results, Lane 1 represents the DNA marker, Lane 2 corresponds to the naked GFP-plasmid, while Lanes 3–7 display polyplexes with a plasmid/NPs ratio of 100, subjected to different concentrations of heparin ranging from 50, 500, 1000, 2500, to 5000 IU/ml, respectively. As shown in Fig. 4**C**, the absence of detectable plasmid bands in the gel lanes where the GFP-plasmid was preserved within the nanosystem is a significant finding. This outcome suggests that the nanosystem exhibits a remarkable capacity to bind and protect the loaded plasmid DNA. This is a critical attribute for any gene delivery

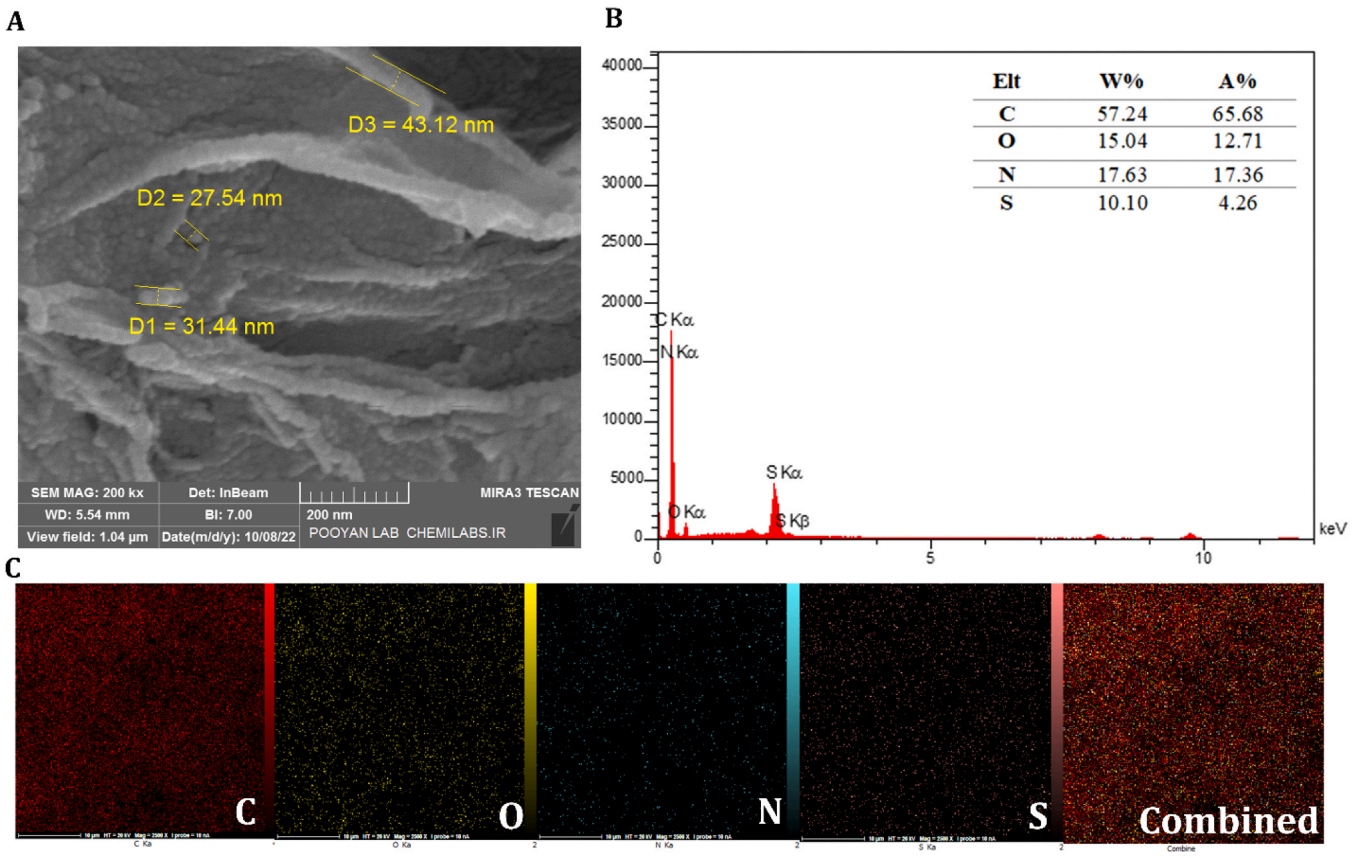

Fig. 3. Characterization of the final nanoconjugate (MCM@CS@PEG-APT(DOX)) through FE-SEM imaging and elemental analysis: **(A)** FE-SEM image displaying the final nanosystem with an average size of 34 nm, **(B)** Elemental composition percentage within the nanosystem, and **(C)** Surface element distribution, including Carbon (C), Oxygen (O), Nitrogen (N), Sulfur (S), and combined elements.

system intended for biomedical applications, as it underlines the nanosystem's ability to protection the genetic material from potential degradation. In fact, the competition between heparin and the nanosystem for binding sites on the plasmid DNA is a central aspect of this experiment. Heparin, due to its negatively charged nature, competes for binding with positively charged components within the nanosystem, such as cationic polymers or other DNA-binding moieties. The fact that the plasmid DNA remained securely encapsulated within the nanosystem, even when exposed to varying concentrations of heparin, implies the robustness of the nanosystem's plasmid-binding properties. This robust binding capability is indicative of the nanosystem's stability and its potential to navigate the challenges posed by the complex biological environment of the human body [38].

Overall, these results signify that the designed polyplexes hold great promise for effective gene delivery applications within the human body. Their ability to withstand the degradative effects of various nucleases, such as DNase I, as well as heparin suggests that they can protect DNA payloads during transit through bodily fluids and tissues, ultimately enhancing the success of gene therapy.

3.3. Cell compatibility study

The assessment of biocompatibility is a pivotal aspect in the development of nanosystems for targeted drug delivery and gene therapy applications. In this study, an MTT assay was conducted to evaluate the specific cell toxicity and targeted drug delivery capabilities of the nanosystem, providing valuable insights into its potential for biomedical application.

In this investigation, MCM@CS@PEG-APT, MCM@CS@PEG-APT (DOX-GFP), and pure DOX were exposed to MCF-7 cell line, as positive overexpressing MUC-1, for 24 and 48 h. As depicted in Fig. 5**A**, treated cell line displayed no significant signs of toxicity when exposed to varying concentrations of MCM@CS@PEG-APT at both 24 and 48-hour intervals. These findings highlight the remarkable biocompatibility of the synthesized nanoconjugate. This biocompatibility is of paramount importance as it underscores the nanosystem's compatibility with living cells, a prerequisite for any viable drug delivery carrier.

Besides, the assessment of cytotoxicity for pure DOX and MCM@CS@PEG-APT (DOX-GFP), as illustrated in Fig. 5**B**, further emphasizes the nanosystem's potential as an effective cancer nanocarrier. Notably, parent DOX, as the positive control, exhibited cytotoxicity on the MCF-7 cell line, consistent with its well-known chemotherapeutic effects. However, the cytotoxicity of MCM@CS@PEG-APT (DOX-GFP) was notably lower, measuring approximately 28.51% and 39.29% at 24 and 48 hours, respectively. These results indicate that the nanosystem efficiently delivers chemotherapeutic drugs to the intended tumor cells while mitigating potential adverse effects. This is a critical advantage, as it suggests that the nanosystem can enhance the therapeutic index of chemotherapeutic agents, reducing off-target toxicity to healthy tissues.

Furthermore, the observed differences in toxicity at two-time intervals when using a Plasmid:NPs ratio of 1:100 are intriguing. This concentration of the nanoconjugate was identified as the optimal concentration for further investigations, signifying its potential for controlled and targeted drug delivery.

3.4. pH-dependent DOX release and kinetics study

The pH-responsive release of DOX was investigated under two distinct pH conditions, namely pH 7.4, representative of physiological conditions, and pH 5.5, mimicking the acidic environment typically

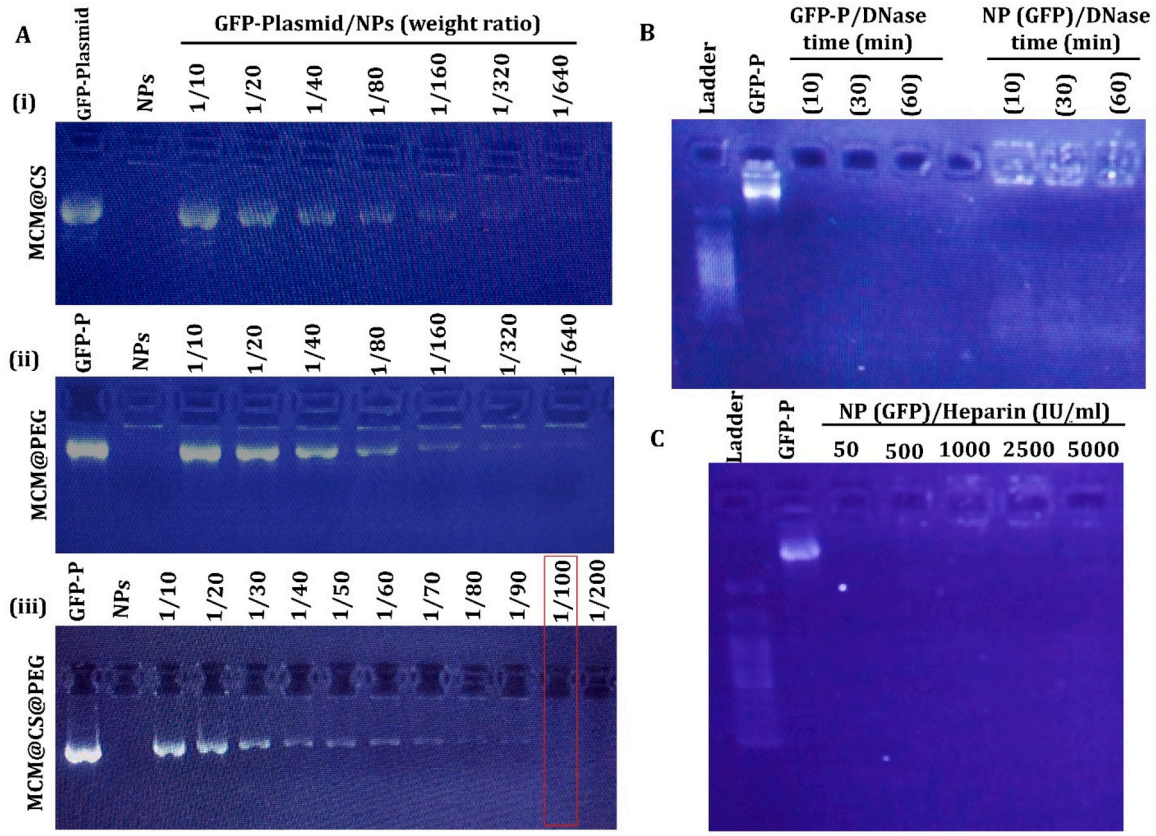

Fig. 4. **(A)** Gel Electrophoresis Examination of Plasmid Binding with Nanoparticles: (i) MCM@CS, (ii) MCM@PEG, and (iii) MCM@CS@PEG in a 1% agarose gel. A GFP-plasmid, and NPs (MCM@CS@PEG) were used as references. **(B)** DNase I Protection Assay: Gel Line 1: DNA marker; Line 2: Naked GFP-plasmid; Line 3, 4, and 5: Naked GFP-plasmid treated with DNase I for 10, 30, and 60 minutes, respectively; Line 7, 8, and 9: Polyplex with GFP plasmid/NPs ratio of 100 treated with DNase I for 10, 30, and 60 minutes, respectively. **(C)** Heparin Competition Assay of MCM@CS@PEG (GFP) Polyplexes: Gel Line 1: DNA marker; Line 2: Naked GFP-plasmid; Line 3–7: Polyplex with plasmid/NPs ratio of 100 subjected to different concentrations of heparin (50, 500, 1000, 2500, 5000 IU/ml).

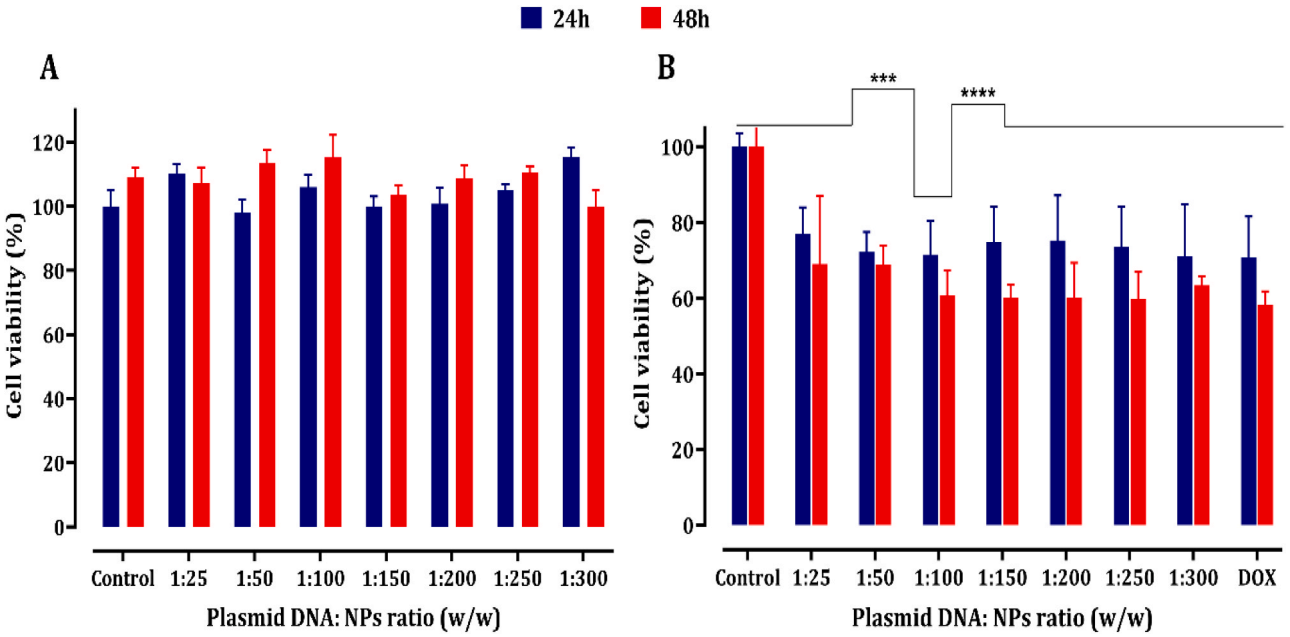

Fig. 5. Cell Viability Assay of MCF-7 (MUC-1 Positive Cells): **(A)** Treatment with different plasmid DNA/NPs ratios using MCM@CS@PEG-APT, and **(B)** Treatment with MCM@CS@PEG-APT (DOX-GFP) and pure DOX, all at a concentration of 50 μg/ml, assessed at two intervals of 24 and 48 hours. Each experiment was conducted three times, and the results are presented as means ± SD. Significant differences are indicated by *"****P value < 0.0001" and "***P value < 0.0007"*.

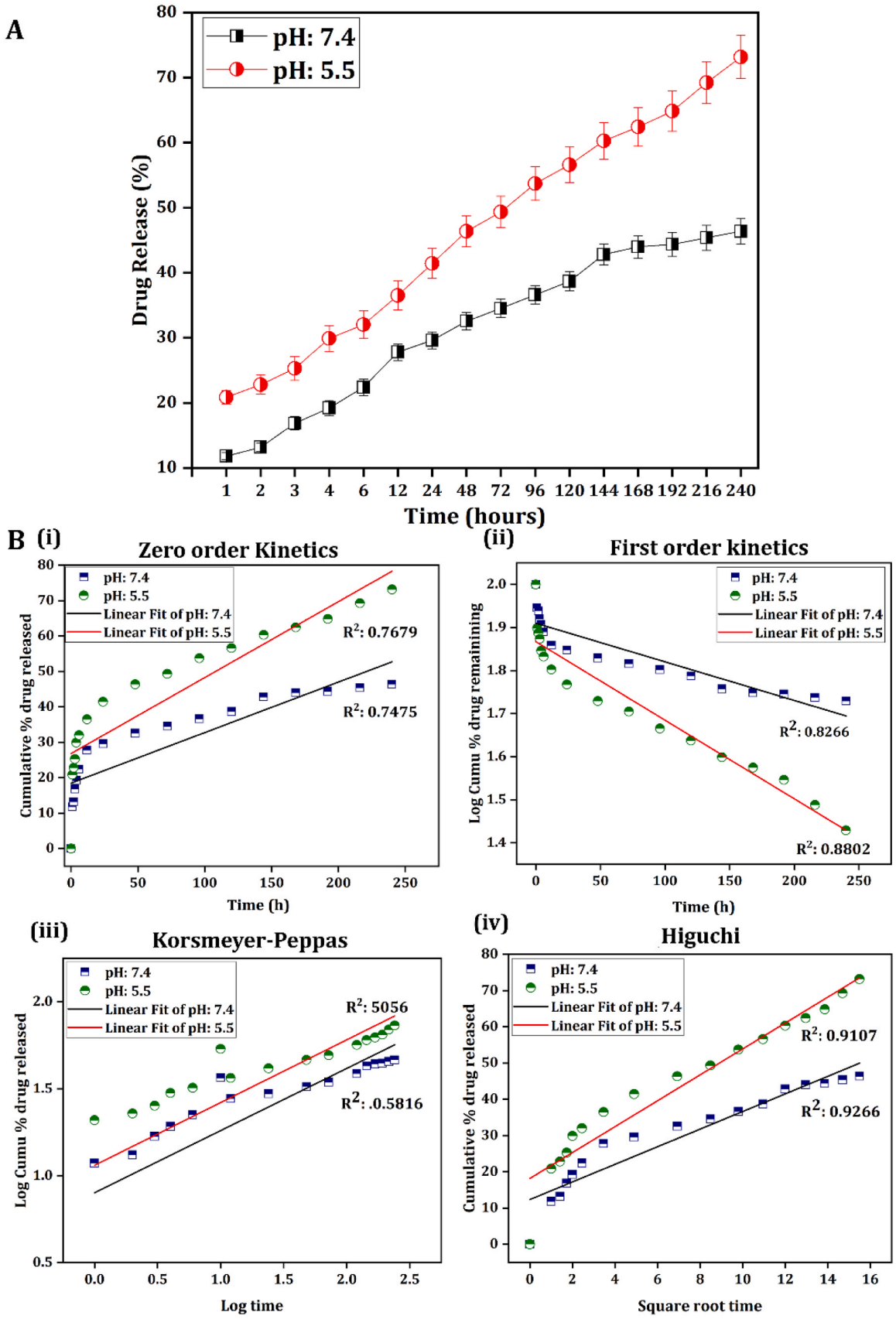

Fig. 6. . (A) Drug release profiles of the nanosystem at two distinct pH values: 5.5 and 7.4. **(B)** Utilization of various kinetic models (Zero Order, First Order, Korsmeyer-Peppas, and Higuchi) to investigate the mechanism of DOX release.

found in malignant tumor tissues (Fig. 6**A**). The release pattern can be described into two phases: (i) Burst Release: Occurring within the initial twelve hours, this phase involves the release of physically associated DOX located on the surface of the nanoconjugate. (ii) Sustained Release: This phase is associated with the gradual release of DOX molecules encapsulated within the pores of MCM-41 and those situated between the two strands of the aptamer.

A total drug release of 46% and 73% was achieved over 10 days at pH values of 7.4 and 5.5, respectively. The release mechanism of DOX from MCM@CS@PEG-APT can be explained based on the structural response of chitosan and the double strands of DNA aptamer within the nanosystem in response to changes in pH. Specifically, the amino groups ($–NH_2$) present on chitosan molecules and DOX undergo protonation at acidic pH levels, resulting in the formation of a cationic polyelectrolyte nature for chitosan [39]. Therefore, the hydrophobicity and solubility of DOX increase, while the hydrophobic interaction between DOX and nano-conjugate reduces.

The study of kinetic drug release holds paramount importance in the development of drug delivery systems, as it provides valuable insights into the controlled release of therapeutic agents. In this study, a comprehensive analysis of various kinetic models was employed to investigate the release behavior of DOX from the nanoconjugate. The selected models included the Zero order, First order, Korsmeyer-Peppas, and Higuchi models, each offering distinct insights into the underlying release mechanisms. The modeling parameters and their corresponding values are summarized in Table 4.

Notably, choosing the most suitable mathematical model contributes to achieving the highest degree of correlation coefficient, which accurately reflects the drug release kinetics. In our investigation, it was evident that the Higuchi square root model [pH 7.4 ($R^2 = 0.92$) and pH 5.5 ($R^2 = 0.91$)] exhibited the best fit when compared to other kinetic models. Consequently, it can be concluded that the release profile of the nanosystem predominantly follows a diffusion mechanism. This implies that the release kinetics of MCM@CS@PEG-APT (DOX) are rely on both the diffusion rate and the gradual degradation of the nanosystem components [40]. Notably, previous research has also reported the applicability of this model to spherical systems, highlighting its relevance in characterizing the slow-release kinetics of DOX [41–43].

On the other hand, it is crucial to note that the mechanism of drug release is influenced by several factors, such as the type of modification (e.g. polymer composition), the drug's own characteristics, and the properties of the materials used in the nanosystem [44]. In our study, the release rate of DOX from MCM@CS@PEG-APT nanoparticles is moderated owing to the presence of copolymerization on the nanoparticle surface. This copolymerization leads to an extended diffusion rate of DOX, allowing it to migrate from one site to another, thereby contributing to the observed gradual and sustained release behavior.

Additionally, the structural behavior of the double-stranded DNA (dsDNA) aptamer at different pH values influences the release mechanism of DOX from the MCM@CS@PEG-APT nanosystem in addition to the pH environment [45]. This process involves the penetration of the pH medium, dissolution of DOX, and gradual leaching of DOX through the interstitial pores of MCM-41, as well as between the two strands of the aptamers. The release rate follows a proportionality to the square root of time, highlighting the complex interplay of multiple factors within the drug release mechanism.

Overall, these findings indicate the slow-release pattern of the nanoconjugate, with its tumor-targeting capabilities and controlled drug release, has the potential to reduce the side effects associated with conventional chemotherapy.

Table 4
Results of different kinetics models in terms of K, slope, and R^2.

Kinetics Model	pH: 7.4			pH: 5.5		
	K	Slope	R^2	K	Slope	R^2
Zero order	0.1698	17.531	0.7475	0.2382	25.994	0.7679
First order	-0.0009	1.9099	0.8266	-0.0019	1.8682	0.8802
Korsmeyer-Peppas	0.3575	0.9017	0.5816	0.3753	1.0502	0.5076
Higuchi	0.3709	-3.8586	0.9266	0.2488	-3.8639	0.901

3.5. Cellular uptake of GFP-plasmid and DOX

To investigate the targeted GFP-plasmid transfection and targeted drug delivery, fluorescent microscopy and flow cytometry were used. Fig. 7 presents both fluorescent and visible light microscopy images, showing GFP expression in plasmids following the uptake of polyplexes and lipofectamine reagent by MCF-7 cells after 24 hours. As illustrated in Fig. 7**A**, the nanosystem MCM@CS@PEG-APT as a negative control, did not exhibit any detectable fluorescent intensity after incubation. This observation is significant and aligns with the results obtained from flowcytometry. In contrast, the fluorescent intensity observed in MCF-7 cells transfected with lipofectamine, the positive control, clearly demonstrates successful GFP expression in the cells. It is noteworthy that the transfection efficiency of the synthesized polyplex was observed to be lower than that achieved with Lipofectamine, but this reduction was not significant (p value>0/05). This finding highlights the potential for achieving better transfection outcomes and suggests that further refinement of the MCM@CS@PEG-APT polyplex system may be necessary to match or exceed the efficiency of lipofectamine as a well-known reference.

Furthermore, to assess the targeted drug delivery capabilities of the synthesized nanosystem, a cellular uptake study was conducted to elucidate the internalization of DOX within the loaded nanosystem. The aptamer exhibits a strong affinity for the MUC-1 receptor, enabling specific binding to the target. In the context of the slightly acidic pH environment surrounding tumor cells, this high-affinity interaction prompts the separation of the double strands of the aptamer, ultimately facilitating drug release. As depicted in Fig. 7**B**, the nanosystem did not exhibit any discernible fluorescence signal. This observation holds profound significance, confirming the validity of the nanosystem as a negative control. In contrast, the internalization of pure DOX, a well-established chemotherapeutic agent, served as the positive control in our study. The resulting images displayed a robust and high-intensity red fluorescence, confirming the successful internalization of DOX. In the following, DOX loaded into the nanosystem exhibited a comparably high red fluorescence intensity. This result is of great significance, as it highlights the capability of the nanosystem to efficiently encapsulate and deliver the therapeutic payload, DOX, to the target cells.

Furthermore, for a quantitative assessment of cellular uptake, the measurements of fluorescence intensity was performed, evaluating both the GFP-expressing plasmid and DOX. This analysis was performed using flow cytometry after a 24-hour incubation period with MCF-7 cells. Flow cytometric analysis revealed that Lipofectamine achieved a transfection rate of approximately 38%, while the polyplexes carrying GFP achieved a transfection efficiency of approximately 31% **(**Fig. 8**)**. Although lipofectamine is a popular and effective transfection reagent, its drawbacks, including cytotoxicity, short-term transgene expression, and the risk of immune reactions, underscore the necessity for developing alternative delivery methods [46,47]. The nanosystem MCM@CS@PEG-APT presents several advantages, including reduced cytotoxicity, the potential for long-term gene expression, and customization for specific applications. Although, there was no significant difference in transfection efficiency between two groups, ongoing refinement and optimization efforts will be the priority of the next research. By addressing these challenges, the nanosystem can potentially become a superior choice for gene delivery and targeted therapy in breast cancer and beyond.

According to literatures, it is demonstrated that chitosan-based polyplexes with a molecular weight (Mw) of 50 kDa or less exhibit notably high transfection efficiency. This phenomenon can be attributed to the

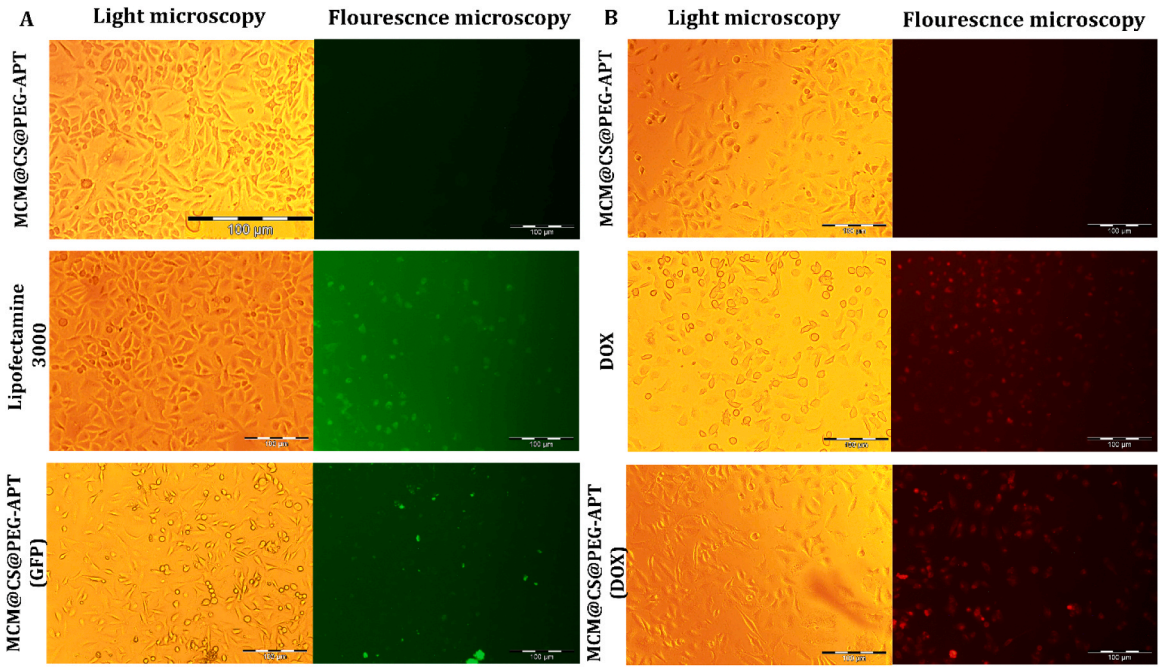

Fig. 7. Fluorescent and Light Microscopy Images of Transfected MCF-7 Cells: **(A)** Displaying fluorescent and light intensity images of cells transfected with MCM@CS@PEG-APT, Lipofectamine 3000-GFP plasmid, and MCM@CS@PEG-APT (GFP) polyplex at 24 hours post-transfection. **(B)** Showing fluorescent and light intensity images of cells treated with MCM@CS@PEG-APT, pure DOX, and MCM@CS@PEG-APT (DOX) at 24 hours post-treatment. The data are representative of three independent biological experiments, with three replicates in each experiment. Scale bar, 100 µm.

inverse relationship between the molecular weight of chitosan and the polyplex's ability to release plasmids [48]. As the molecular weight of chitosan increases, the capacity of the polyplex to effectively release plasmids decreases. Conversely, polyplexes with a molecular weight as low as 5 kDa demonstrate significantly reduced transfection efficiency, primarily due to their limited capacity to bind effectively with plasmids [49]. In this work, we have used a medium molecular weight of chitosan, striking a balance that allows to optimize transfection efficiency. Similarly, in a recent study researchers employed a carrier derived from chitosan polyplex, which modified by introducing hyaluronic acid-conjugated triptorelin as targeting agents [16]. This nanocarrier was utilized for the delivery of CRISPR/Cas9 plasmids, resulting in a transfection efficiency of approximately 22%. However, in our current study, we innovatively employed the co-polymerization of chitosan and PEG. This strategic modification substantially enhanced the plasmid delivery efficiency, achieving an impressive transfection rate of 31%. This outcome serves as evidence to the remarkable efficacy of the designed nanosystem.

On the other hand, to determine the targeting properties of MCM@CS@PEG-APT (DOX) and drug delivery efficiency, the MCF-7 tumor cell line has been treated with both pure DOX and drug-loaded carrier (MCM@CS@PEG-APT (DOX)). Flow cytometry analysis was applied to evaluate the nanoconjugate uptake by the MUC1-positive cells. As shown in Fig. 8, 95% of free drug was uptake by cells based on the fluorescent signals generated by pure DOX, whereas the drug uptake of MCM@CS@PEG-APT (DOX) for MUC-1-positive cells is about 98%. Thus, these results confirm that MCM@CS@PEG-APT (DOX) is selectively taken up by the MUC-1-positive tumor cells, and the intercalation of DOX within the MUC-1 aptamer does not affect its binding properties. In our recent work, we developed a nanocarrier based on graphene oxide graphene oxide, strategically functionalized with PEG, gold nanoparticles and incorporating MUC-1 aptamer [50]. This approach successfully facilitated the delivery of DOX into breast tumor cells, yielding an impressive efficiency rate of approximately 54.10%. However, the novel nanosystem developed in this current study represents a significant advancement. It has demonstrated an exceptional capability to enhance the delivery of DOX, achieving an outstanding efficiency rate of up to 95%. These findings are pivotal in advancing the development of this nanosystem as a promising tool in cancer therapy, offering improved precision and safety in the delivery of chemotherapeutic agents.

3.6. Co-delivery study

A significant aspect of the study involved the co-delivery of two vital agents, GFP plasmid and DOX, using the innovative nanosystem MCM@CS@PEG-APT. Co-delivery is particularly persuasive as it opens up possibilities for multifunctional therapeutic strategies. To assess the co-delivery efficiency, we utilized fluorescence microscopy and flow cytometry to analyze the extent to which cells simultaneously contained both GFP-plasmid and DOX, shedding light on the nanosystem's ability to transport multiple payloads concurrently.

Fluorescence microscopy images obtained from transfected MCF-7 cells revealed distinct green and red fluorescence signals, corresponding to GFP-plasmid and DOX, respectively (Fig. 9**A**). These findings provide visual confirmation of the successful co-delivery of both plasmid and drug by the nanosystem. Flow cytometry results further substantiated this co-delivery efficiency, demonstrating that 42.7% of cells exhibited the presence of both GFP-plasmid and DOX, while 52.2% of cells exclusively contained DOX (Fig. 9**B**). This outcome underlines the nanosystem's competence in orchestrating the simultaneous delivery of multiple therapeutic agents, a capability with far-reaching implications for advancing therapeutic outcomes. Remarkably, cells treated with MCM@CS@PEG-APT, employed as a negative control, exhibited negligible fluorescence intensity in both fluorescent channels (FL-1 and FL-2). This observation is of particular significance as it highlights the nanosystem's specificity and efficiency in selectively delivering therapeutic agents, reinforcing its potential for applications requiring synergistic therapeutic actions and precise targeting for enhanced therapeutic efficacy.

The ability to co-deliver therapeutic agents holds immense promise for cancer therapy. In the context of breast cancer, for instance, co-

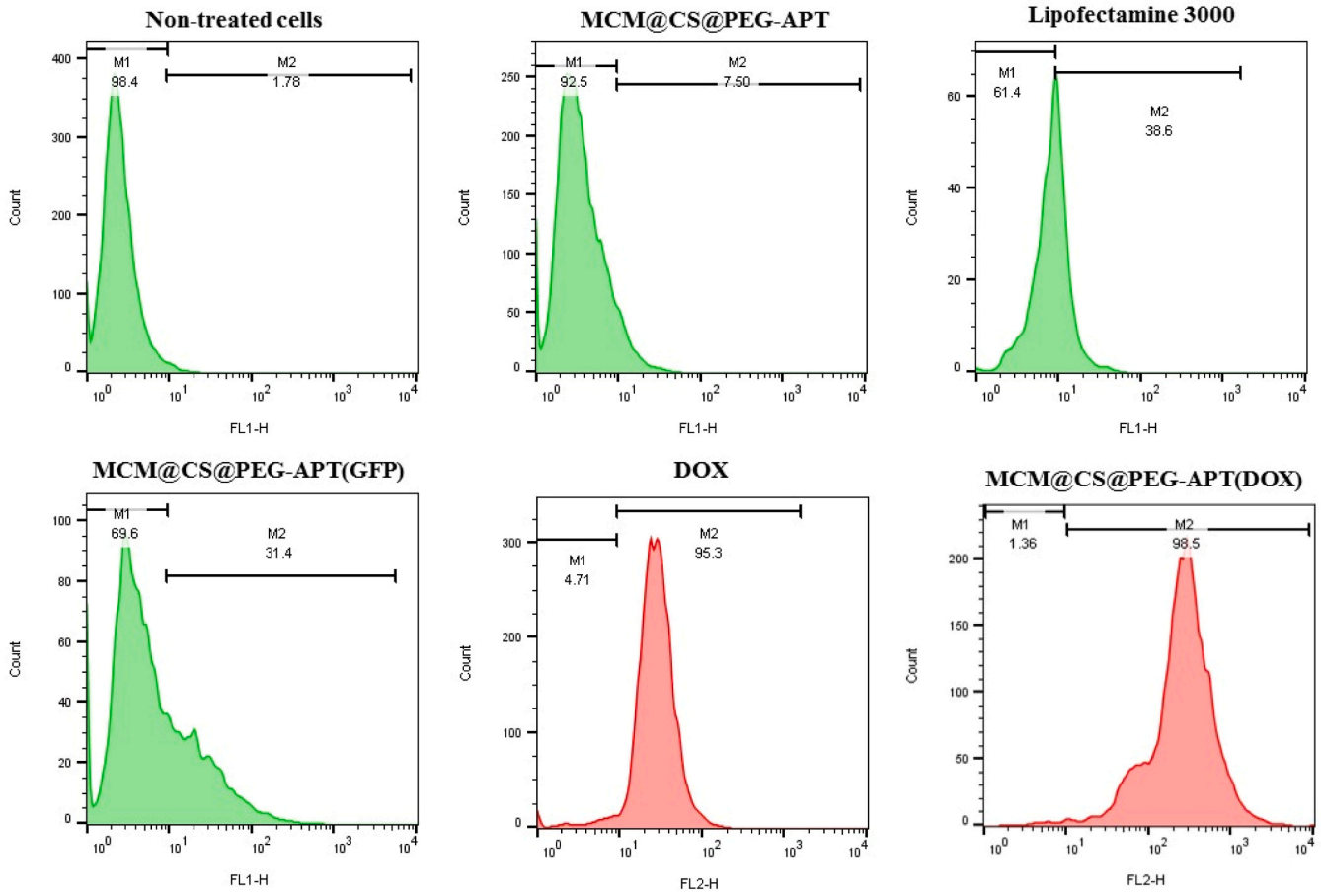

Fig. 8. Analyzes the transfection efficiency of targeted polyplexes using GFP protein expression in MCF-7 and compares their efficiency with Lipofectamine3000-GFP plasmid, and targeted nanosystem encapsulated DOX in MCF-7 and compares their efficiency with pure DOX. The data are representative of three independent biological experiments, with three replicates in each experiment.

delivery can offer synergistic effects. GFP plasmid, a gene expression marker, provides valuable insights into cellular behavior, enabling real-time monitoring of transfection efficiency. Simultaneously, DOX, a potent chemotherapeutic agent, targets and eradicates cancer cells. By delivering these agents together, our nanosystem presents the opportunity to combine gene expression monitoring and chemotherapy within a single platform. This not only enhances the precision of cancer therapy but also provides a means to tailor treatment strategies based on real-time feedback.

4. Conclusion

In summary, our study has successfully developed and characterized the MCM@CS@PEG-APT nanosystem for targeted co-delivery of plasmid DNA and DOX to breast cancer cells. Through comprehensive experiments, it was demonstrated that this innovative nanocarrier efficiently encapsulates and delivers both genetic material and chemotherapeutic agents, indicating a notable loading capacity of 99.42% for DOX at a 1:1 nanosystem to drug ratio. This high loading efficiency is complemented by the nanosystem's pH-responsive release behavior, which significantly enhances drug delivery to the acidic microenvironment of tumors, with a total release of 73% at pH 5.5 over 10 days compared to 46% at physiological pH (7.4).

Furthermore, the cellular uptake studies revealed a remarkable efficiency, with 98% of the targeted cells internalizing the DOX-loaded nanosystem, underscoring its precision in reaching and affecting cancer cells. The nanosystem's ability to co-deliver DOX and plasmid DNA was confirmed through fluorescence microscopy and flow cytometry, with 42.7% of cells exhibiting both GFP and DOX signals. This indicates not only the nanosystem's capacity to transport multiple therapeutic agents simultaneously but also its potential to enable synergistic treatment strategies. important, the nanosystem demonstrated excellent biocompatibility, with significantly lower cytotoxicity observed in MCF-7 cells treated with MCM@CS@PEG-APT (DOX-GFP) compared to pure DOX, highlighting its safety profile and the reduced risk of adverse effects.

Overall, the MCM@CS@PEG-APT nanosystem represents a significant advancement in the field of targeted cancer therapy, offering a multifunctional platform for the precise and efficient delivery of therapeutic agents. Its development paves the way for more effective, personalized treatment strategies, marking a crucial step towards the realization of precision medicine in cancer care. As we move forward, our focus will be on further optimizing this nanosystem and exploring its applicability across a broader range of cancer types, aiming to bring this promising technology closer to clinical application.

CRediT authorship contribution statement

Ilnaz Rahimmanesh: Writing – review & editing, Writing – original draft, Validation, Methodology, Investigation, Formal analysis, Conceptualization. **Elham Bidram:** Writing – review & editing, Writing – original draft, Visualization, Validation, Supervision, Methodology, Investigation, Formal analysis, Conceptualization. **Saeed Karbasi:** Writing – review & editing, Writing – original draft, Software, Methodology, Investigation, Formal analysis, Conceptualization. **Mohammad Rafienia:** Writing – review & editing, Writing – original draft,

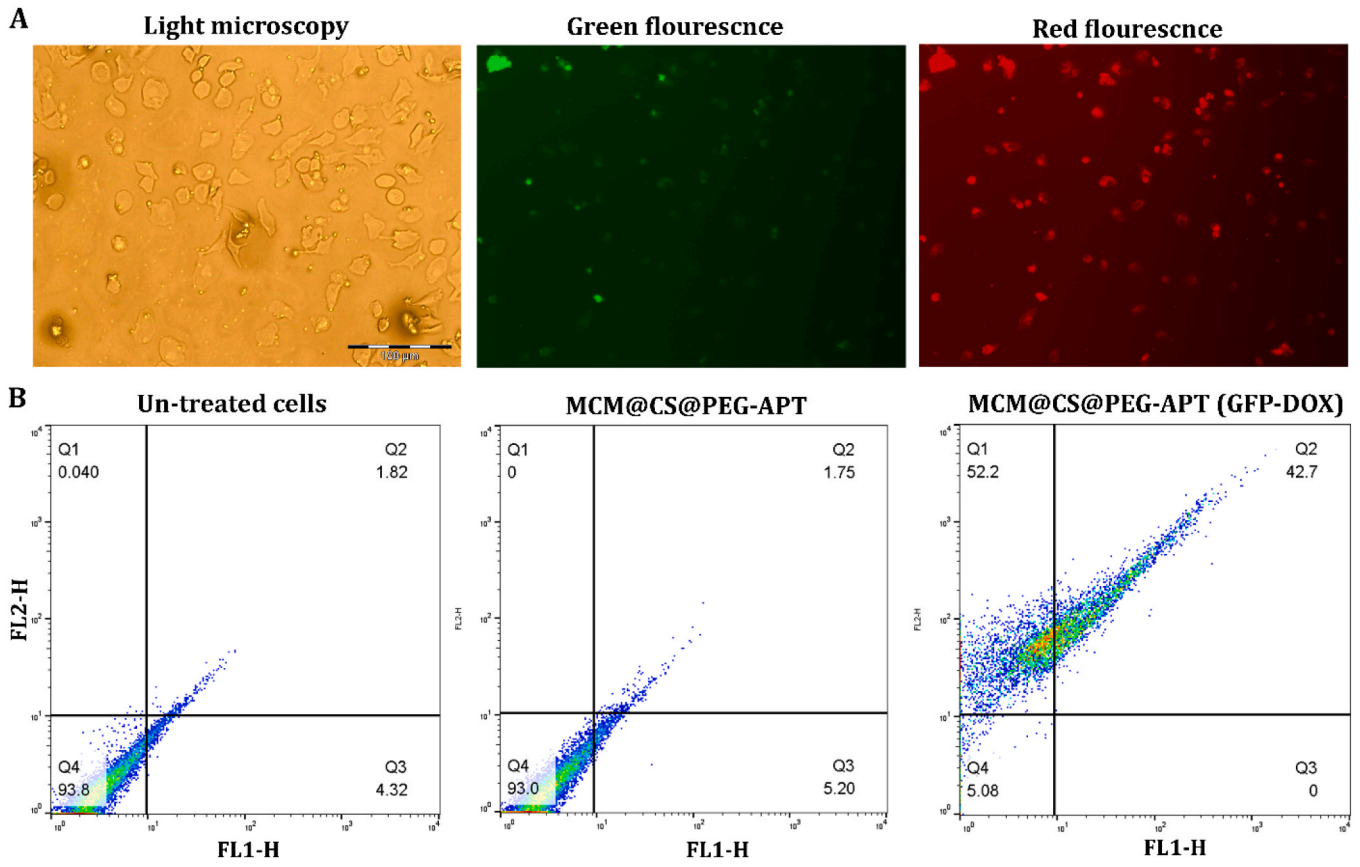

Fig. 9. Assessing the Co-Delivery of GFP-Plasmid and DOX via the MCM@CS@PEG-APT Nanosystem: **(A)** Fluorescence microscopy images captured from MCF-7 cells treated with MCM@CS@PEG-APT (GFP-DOX) after 24 hours. **(B)** Flow cytometry analysis comparing untreated cells, MCM@CS@PEG-APT without cargo, and MCM@CS@PEG-APT (GFP-DOX) after 24 hours in MCF-7 cells. The data are representative of three independent biological experiments, with three replicates in each experiment. Scale bar, 100 μm.

Visualization, Validation. **Shaghayegh Haghjooy Javanmard:** Writing – review & editing, Writing – original draft, Visualization, Validation. **Yavuz Nuri Ertas:** Writing – review & editing, Writing – original draft, Visualization, Validation. **Ali Zarrabi:** Writing – review & editing, Writing – original draft, Visualization, Validation. **Laleh Shariati:** Writing – review & editing, Writing – original draft, Visualization, Validation, Supervision, Project administration, Methodology, Investigation, Funding acquisition, Formal analysis, Conceptualization. **Yasaman Esmaeili:** Writing – review & editing, Writing – original draft, Software, Methodology, Formal analysis, Data curation, Conceptualization. **Arezou Dabiri:** Writing – review & editing, Writing – original draft, Software, Methodology, Investigation, Formal analysis, Conceptualization. **Fariba Mashayekhi:** Writing – review & editing, Visualization, Validation, Methodology, Formal analysis.

Declaration of Competing Interest

The authors declare the following financial interests/personal relationships which may be considered as potential competing interests: Laleh Shariati reports financial support was provided by Isfahan University of Medical Sciences. Laleh Shariati reports a relationship with Isfahan University of Medical Sciences that includes: employment. If there are other authors, they declare that they have no known competing financial interests or personal relationships that could have appeared to influence the work reported in this paper.

Data availability

Data will be made available on request.

Acknowledgments

We are deeply grateful to Isfahan University of Medical Sciences, Deputy of Research, for their support (Grant No 199653 & 3400772).

References

[1] R.A. Dar, M. Rasool, A. Assad, Breast cancer detection using deep learning: datasets, methods, and challenges ahead, Comput. Biol. Med. (2022) 106073.
[2] C.H. Barrios, Global challenges in breast cancer detection and treatment, Breast 62 (2022) S3–S6.
[3] M. Li, Z. Ma, M. Peng, L. Li, M. Yin, S. Yan, J. Shen, A gene and drug co-delivery application helps to solve the short life disadvantage of RNA drug, Nano Today 43 (2022) 101452.
[4] Y. Esmaeili, A. Farazin, I. Rahimmanesh, A. Bigham, Gene Delivery, (2023).
[5] C. Zhao, X. Ling, Y. Xia, B. Yan, Q. Guan, LncRNA UCA1 promotes SOX12 expression in breast cancer by regulating m6A modification of miR-375 by METTL14 through DNA methylation, Cancer gene Ther. 29 (2022) 1043–1055.
[6] Sl Ghaedamini, B. Hashemibeni, A. Honarvar, A. Rabiei, S. Karbasi, Recent innovations in strategies for breast cancer therapy by electrospun scaffolds: a review, J. Polym. Environ. (2023) 1–27.
[7] X. Wang, C. Li, Y. Wang, H. Chen, X. Zhang, C. Luo, W. Zhou, L. Li, L. Teng, H. Yu, Smart drug delivery systems for precise cancer therapy, Acta Pharm. Sin. B (2022).
[8] M. Dymek, E. Sikora, Liposomes as biocompatible and smart delivery systems–the current state, Adv. Colloid Interface Sci. (2022) 102757.
[9] B. Tian, J. Liu, Smart stimuli-responsive chitosan hydrogel for drug delivery: A review, Int. J. Biol. Macromol. (2023) 123902.
[10] A. Srivastav, K. Gupta, D. Chakraborty, P. Dandekar, R. Jain, Efficiency of chitosan-coated PLGA nanocarriers for cellular delivery of SiRNA and CRISPR/Cas9 complex, J. Pharm. Innov. (2020) 1–14.
[11] Y. Zhou, G. Quan, Q. Wu, X. Zhang, B. Niu, B. Wu, Y. Huang, X. Pan, C. Wu, Mesoporous silica nanoparticles for drug and gene delivery, Acta Pharm. Sin. B 8 (2018) 165–177.
[12] Y. Zhao, J.L. Vivero-Escoto, I.I. Slowing, B.G. Trewyn, V.S. Lin, Capped mesoporous silica nanoparticles as stimuli-responsive controlled release systems for intracellular drug/gene delivery, Expert Opin. Drug Deliv. 7 (2010) 1013–1029.

[13] Y. Esmaeili, M. Khavani, A. Bigham, A. Sanati, E. Bidram, L. Shariati, A. Zarrabi, N. A. Jolfaie, M. Rafienia, Mesoporous silica@ chitosan@ gold nanoparticles as "on/off" optical biosensor and pH-sensitive theranostic platform against cancer, Int. J. Biol. Macromol. 202 (2022) 241–255.
[14] S. He, Y. Du, H. Tao, H. Duan, Advances in aptamer-mediated targeted delivery system for cancer treatment, Int. J. Biol. Macromol. (2023) 124173.
[15] S.A. Moosavian, P. Kesharwani, V. Singh, A. Sahebkar, Aptamer-functionalized liposomes for targeted cancer therapy, Aptamers Eng. Nanocarriers Cancer Ther. (2023) 141–172.
[16] N. Tavazohi, M. Mirian, J. Varshosaz, S. Shirani-Bidabadi, H.M.M. Sadeghi, H. Khanahmad, Fabrication and evaluation of a dual-targeting nanoparticle mediated CRISPR/Cas9 delivery to combat drug resistance in breast cancer cells, J. Drug Deliv. Sci. Technol. (2023) 104628.
[17] B.L. Santini, M. Zúñiga-Bustos, A. Vidal-Limon, J.B. Alderete, S.A. Águila, V. A. Jiménez, In silico design of novel mutant anti-MUC1 aptamers for targeted cancer therapy, J. Chem. Inf. Model. 60 (2019) 786–793.
[18] S. Shahrad, M. Rajabi, H. Javadi, A.A. Karimi Zarchi, M.H. Darvishi, Targeting lung cancer cells with MUC1 aptamer-functionalized PLA-PEG nanocarriers, Sci. Rep. 12 (2022) 4718.
[19] Y. Esmaeili, A. Zarrabi, S.Z. Mirahmadi-Zare, E. Bidram, Hierarchical multifunctional graphene oxide cancer nanotheranostics agent for synchronous switchable fluorescence imaging and chemical therapy, Microchim. Acta 187 (2020) 1–15.
[20] Y. Esmaeili, H.S. Ghaheh, F. Ghasemi, L. Shariati, M. Rafienia, E. Bidram, A. Zarrabi, Graphene oxide quantum dot-chitosan nanotheranostic platform as a pH-responsive carrier for improving curcumin uptake internalization: In vitro & in silico study, Biomater. Adv. 139 (2022) 213017.
[21] S. Noreen, A. Maqbool, I. Maqbool, A. Shafique, M.M. Khan, Y. Junejo, B. Ahmed, M. Anwar, A. Majeed, M. Abbas, Multifunctional mesoporous silica-based nanocomposites: Synthesis and biomedical applications, Mater. Chem. Phys. 285 (2022) 126132.
[22] F. Ahmadi, A. Sodagar-Taleghani, P. Ebrahimnejad, S.P.H. Moghaddam, F. Ebrahimnejad, K. Asare-Addo, A. Nokhodchi, A review on the latest developments of mesoporous silica nanoparticles as a promising platform for diagnosis and treatment of cancer, Int. J. Pharm. (2022) 122099.
[23] A.I. Fahira, R. Amalia, M.I. Barliana, V.A. Gatera, R. Abdulah, Polyethyleneimine (PEI) as a polymer-based co-delivery system for breast cancer therapy, Breast Cancer.: Targets Ther. (2022) 71–83.
[24] S. He, F. Gao, J. Ma, H. Ma, G. Dong, C. Sheng, Aptamer-protac conjugates (apcs) for tumor-specific targeting in breast cancer, Angew. Chem. 133 (2021) 23487–23493.
[25] A. Sheikh, S. Md, P. Kesharwani, Aptamer grafted nanoparticle as targeted therapeutic tool for the treatment of breast cancer, Biomed. Pharmacother. 146 (2022) 112530.
[26] N. Ahmadi Nasab, H. Hassani Kumleh, M. Beygzadeh, S. Teimourian, M. Kazemzad, Delivery of curcumin by a pH-responsive chitosan mesoporous silica nanoparticles for cancer treatment, Artificial cells, Nanomed., Biotechnol. 46 (2018) 75–81.
[27] R.S. Nair, A. Morris, N. Billa, C.-O. Leong, An evaluation of curcumin-encapsulated chitosan nanoparticles for transdermal delivery, Aaps Pharmscitech 20 (2019) 1–13.
[28] M.K.M. Esfahani, S.E. Alavi, P.J. Cabot, N. Islam, E.L. Izake, PEGylated Mesoporous Silica Nanoparticles (MCM-41): A promising carrier for the targeted delivery of fenbendazole into prostrate cancer cells, Pharmaceutics 13 (2021) 1605.
[29] Z. Hami, S.M. Rezayat, K. Gilani, M. Amini, M. Ghazi-Khansari, In-vitro cytotoxicity and combination effects of the docetaxel-conjugated and doxorubicin-conjugated poly (lactic acid)-poly (ethylene glycol)-folate-based polymeric micelles in human ovarian cancer cells, J. Pharm. Pharmacol. 69 (2017) 151–160.
[30] S.P. Victor, W. Paul, M. Jayabalan, C.P. Sharma, Supramolecular hydroxyapatite complexes as theranostic near-infrared luminescent drug carriers, CrystEngComm 16 (2014) 9033–9042.
[31] R.E. Morsi, M.A. Elsherief, M. Shabaan, M. Elsabee, Chitosan/MCM-41 nanocomposites for efficient beryllium separation, J. Appl. Polym. Sci. 135 (2018) 46040.
[32] Q. Zhang, X. Xu, Y. Liu, M. Xu, S. Deng, Y. Chen, H. Yuan, F. Yu, Y. Huang, K. Zhao, A feasible strategy to balance the crystallinity and specific surface area of metal oxide nanocrystals, Sci. Rep. 7 (2017) 1–12.
[33] M. Popova, N. Koseva, I. Trendafilova, H. Lazarova, V. Mitova, J. Mihály, D. Momekova, G. Momekov, I.Z. Koleva, H.A. Aleksandrov, Tamoxifen delivery system based on PEGylated magnetic MCM-41 silica, Molecules 25 (2020) 5129.
[34] E. Lowry, M. Piri, Effect of surface chemistry on confined phase behavior in nanoporous media: an experimental and molecular modeling study, Langmuir 34 (2018) 9349–9358.
[35] S. Shirani-Bidabadi, M. Mirian, J. Varshosaz, N. Tavazohi, H.M.M. Sadeghi, L. Shariati, Gene network analysis of oxaliplatin-resistant colorectal cancer to target a crucial gene using chitosan/hyaluronic acid/protamine polyplexes containing CRISPR-Cas9, Biochim. Et. Biophys. Acta (BBA)-Gen. Subj. 1867 (2023) 130385.
[36] K.S. Egorova, A.V. Posvyatenko, S.S. Larin, V.P. Ananikov, Ionic liquids: Prospects for nucleic acid handling and delivery, Nucleic Acids Res. 49 (2021) 1201–1234.
[37] B. Gu, M. Smyth, J. Kohanoff, Protection of DNA against low-energy electrons by amino acids: a first-principles molecular dynamics study, Phys. Chem. Chem. Phys. 16 (2014) 24350–24358.
[38] Q. Yu, X. Xiong, L. Zhao, T. Xu, Q. Wang, Antifibrotic effects of specific siRNA targeting connective tissue growth factor delivered by polyethyleneimine-functionalized magnetic iron oxide nanoparticles on LX-2 cells, Mol. Med. Rep. 21 (2020) 181–190.
[39] D. Wu, L. Zhu, Y. Li, X. Zhang, S. Xu, G. Yang, T. Delair, Chitosan-based colloidal polyelectrolyte complexes for drug delivery: a review, Carbohydr. Polym. 238 (2020) 116126.
[40] R. Gouda, H. Baishya, Z. Qing, Application of mathematical models in drug release kinetics of carbidopa and levodopa ER tablets, J. Dev. Drugs 6 (2017) 1–8.
[41] L. Slika, A. Moubarak, J. Borjac, E. Baydoun, D. Patra, Preparation of curcumin-poly (allyl amine) hydrochloride based nanocapsules: Piperine in nanocapsules accelerates encapsulation and release of curcumin and effectiveness against colon cancer cells, Mater. Sci. Eng.: C. 109 (2020) 110550.
[42] M. Mouslmani, J.M. Rosenholm, N. Prabhakar, M. Peurla, E. Baydoun, D. Patra, Curcumin associated poly (allylamine hydrochloride)-phosphate self-assembled hierarchically ordered nanocapsules: size dependent investigation on release and DPPH scavenging activity of curcumin, RSC Adv. 5 (2015) 18740–18750.
[43] O. Nasrallah, R. El Kurdi, M. Mouslmani, D. Patra, Doping of ZnO nanoparticles with curcumin: pH dependent release and DPPH scavenging activity of curcumin in the nanocomposites, Curr. Nanomater. 3 (2018) 147–152.
[44] C. Amgoth, C. Phan, M. Banavoth, S. Rompivalasa, G. Tang, Polymer properties: functionalization and surface modified nanoparticles. in: Role of Novel Drug Delivery Vehicles in Nanobiomedicine, IntechOpen, 2019.
[45] F.R. Wibowo, O.A. Saputra, W.W. Lestari, M. Koketsu, R.R. Mukti, R. Martien, pH-triggered drug release controlled by poly (styrene sulfonate) growth hollow mesoporous silica nanoparticles, ACS Omega 5 (2020) 4261–4269.
[46] W.N. Nakami, J. Nguhiu-Mwangi, A.Ne Kipyegon, M. Ogugo, C. Muteti, S. Kemp, Comparative efficiency for in vitro transfection of goat undifferentiated spermatogonia using lipofectamine reagents and electroporation, Stem Cells Cloning.: Adv. Appl. (2022) 11–20.
[47] Z.X. Chong, S.K. Yeap, W.Y. Ho, Transfection types, methods and strategies: A technical review, PeerJ 9 (2021) e11165.
[48] M. Karayianni, T. Sentoukas, A. Skandalis, N. Pippa, S. Pispas, Chitosan-Based Nanoparticles for Nucleic Acid Delivery: Technological Aspects, Applications, and Future Perspectives, Pharmaceutics 15 (2023) 1849.
[49] Y. Cao, Y.F. Tan, Y.S. Wong, M.W.J. Liew, S. Venkatraman, Recent advances in chitosan-based carriers for gene delivery, Mar. Drugs 17 (2019) 381.
[50] Y. Esmaeili, A. Zarrabi, S.Z. Mirahmadi-Zare, E. Bidram, Hierarchical multifunctional graphene oxide cancer nanotheranostics agent for synchronous switchable fluorescence imaging and chemical therapy, Microchim. Acta 187 (2020) 1–15.